Nanoscale Motion Control With a Compact Minimum-Actuator Magnetic Levitator

Jie Gu

Won-jong Kim[1]
Phone: (979) 845-3645;
Fax: (979) 862-3989;
e-mail: wjkim@mengr.tamu.edu

Shobhit Verma

Department of Mechanical Engineering,
Texas A&M University,
College Station, TX 77843-3123

This paper presents a novel magnetically levitated (maglev) stage developed to meet the ever-increasing precise positioning requirements in nanotechnology. This magnetic levitator has 6 independent linear actuators necessary and sufficient to generate all 6-degree-of-freedom (6-DOF) motions. This minimum-actuator design concept led to a compact, 200 g lightweight moving part and the power consumption less than of a Watt, thereby reducing the thermal-expansion error drastically. The analysis and sizing of the magnetic linear actuators and the working principle of the maglev stage are presented. We designed and implemented stabilizing controllers for 6-DOF motion control with the dynamic model based on the actuator analysis. Test results showed nanoscale step responses in all six axes with 2 nm rms horizontal position noise. A noise propagation model and analysis identified the capacitance sensor noise and the floor vibration as the dominant noise sources in the vertical and horizontal dynamics, respectively. A comparison of noise performances with controllers closed at 25, 65, and 90 Hz crossover frequencies illustrated how the selection of the control bandwidth should be made for nanopositioning. Experimental results including a 250 μm step response, sinusoidal and square-wave trajectories, and spherical motion generation demonstrated the three-dimensional (3D) nanoscale motion-control capability of this minimum-actuator magnetic levitator. Potential applications of this maglev stage include manufacture of nanoscale structures, atomic-level manipulation, assembly and packaging of microparts, vibration isolation for delicate instruments, and seismic motion detection.
[DOI: 10.1115/1.1978906]

Keywords: Nanoscale Motion Control, Real-Time Control, 6-DOF Motion, Noise Propagation and Analysis, Precision Magnetic Levitation

1 Introduction

The demands for high-precision positioning stages have increased dramatically in the last decades. Among many applications that require high-precision positioning, nanomanipulation is one of the most important processes in nanotechnology that enables us to control and fabricate nanoscale objects. A nanomanipulation system must actuate to load, position, and orient nanoscale objects very precisely, and requires high accuracy, long-range motion, multi-DOF motion generation, and wide control bandwidth [1]. However, there are many theoretical and practical challenges in this early nanopositioning and nanomanipulation research stage. Important technical issues include the development of high-precision manipulation methodologies and the tools for specific applications [2].

Nanoparticles and nanorods can be positioned on a surface by mechanical pushing [3]. One of the most widely used nanomanipulation systems is based on the piezoelectric actuation technology [4,5]. However, there are several technical challenges with piezoelectric actuators. (1) The accuracy is greatly influenced by thermal drift under temperature variation. (2) The hysteresis in the piezoelectric materials reduces the repeatability in positioning. (3) A slow creeping motion after a large voltage step results in a significant positioning error [6]. Besides piezoactuation systems, there are other types of positioners including a high-speed precision stage with 0.69 nm resolution using a nonresonant-type ultrasonic motor [7]. However, the motion of this system is limited in only one axis.

A promising solution for nanoscale positioning is the magnetic-levitation technology. It has been successfully implemented in various applications, such as high-speed train suspension, vibration isolation, magnetic bearings, electromagnetic launchers, superconducting gyroscope rotor suspension, and precision positioning [8]. Advantages of the maglev technology include the following. (1) Because there is no friction, no lubricant and precision bearings are needed. As a result, the fabrication cost can be significantly reduced. (2) Without friction, stiction, and backlash, the system dynamics is simple, and the repeatability and resolution is excellent. (3) A single-moving part can produce and control all 6 axis motions without additional linkages. This structural simplicity increases the natural frequencies, which allows a high-bandwidth control, thereby reducing the system response time. (4) The light moving-part mass also leads to low power consumption. (5) It is compatible with clean-room or vacuum environments without particulate generation, which is highly suited for the nanotechnology and semiconductor manufacturing industries.

The maglev technology has been successfully applied in precision motion control. Hajjaji and Ouladsine [9] built a nonlinear control model for long-range movement of a maglev system, and tested it by real-time control implementation. Takahara [10] showed the applicability of a maglev concept in a precision antenna pointing system. Gupta et al. [11] developed a steering mirror. Hollis and Salcudean [12] demonstrated the applicability of maglev instruments in teleoperation, haptic interface devices, and vibration isolation. Salcudean et al. [13] built a 6-DOF gravity cancellation system for aerospace experiments by using maglev technology. Menq et al. [14] achieved the 6-DOF levitation and

[1]Corresponding author, Member of ASME

Contributed by the Dynamic Systems, Measurement, and Control Division of THE AMERICAN SOCIETY OF MECHANICAL ENGINEERS for publication in the ASME JOURNAL OF DYNAMIC SYSTEMS, MEASUREMENT, AND CONTROL. Manuscript received: May 23, 2003; Final revision: August 24, 2004. Associate Editor: Santosh Devasia.

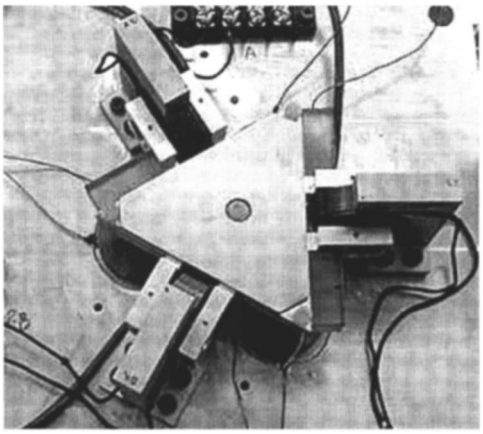

Fig. 1 Photograph of the maglev stage. The triangular shape in the center is the maglev single-moving platen

position control of a 2.4 kg part. A planar maglev positioner with air-core solenoids and permanent magnets was designed by Jung and Baek [15]. This positioner had a lower resolution than the stage presented in this paper.

There are several key aspects regarding possible improvements of the maglev systems developed in previous work—resolution, compactness, response time, and travel range. (1) Chen and Busch-Vishniac [16] constructed a maglev 2 axis probe station with a 200 nm resolution for semiconductor fabrication. However, microelectronic feature sizes shrank into the sub-100 nm realm in recent years. (2) Kim and Trumper [17] developed a maglev stage with 5 nm rms lateral resolution and 25 nm rms vertical resolution using four three-phase levitation motors. Its dynamic performance could have been better if it had had a more compact structure with a minimum number of actuators. For example, the four actuators, each of which provides multiple axes of force, give redundant driving capability and cause a significant coupling to the system. (3) Holmes et al. [18,19] achieved sub-nanometer resolution by floating his stage in oil. However, the bandwidth of such a heavily damped stage was only 1 Hz that made the stage slow in response to motion commands. (4) Most commercially available nanopositioners have a coarse moving stage while their fine travel range is still less than 100 μm. As a result, it is difficult to use such stages to search or scan an area bigger than 100×100 μm without sacrificing resolution or speed.

We herein present a novel 6-DOF maglev-stage design that can overcome the shortcoming of the existing stages. The lightweight, compact, single-moving-part structure with the minimum number of actuators facilitated improved resolution, large bandwidth, increased travel range, and reduced power consumption compared to existing systems. Specifically, the moving-part mass of our stage is 0.2126 kg, and the whole system consumes only 15 mW in each lateral actuator and 320 mW in each vertical actuator in steady state. Our maglev stage achieved the position resolution of 2 nm rms in lateral translation, 25 nm rms in vertical translation, and 300 nrad rms in rotation. This fine position resolution is maintained throughout the 300 μm translational travel ranges and 3.5 mrad angular travel ranges. A 10 ms settling time was obtained by a controller with a 90 Hz crossover frequency. Other notable achievements include 1 m/s maximum speed and 2 g maximum acceleration. Figure 1 is a photograph of the maglev system we developed.

A detailed discussion on the electromechanical design and construction is presented in Sec. 2. An analysis and design of the linear magnetic actuators is given in the later part of the section. Sections 3 and 4 discuss the issues of magnetic actuation force, dynamic modeling, and control system design. Following is a noise propagation model and analysis to determine the contributions of various noise sources given in Sec. 5. Based on this noise analysis, an engineering tradeoff is made to select the optimal control bandwidth. The test results presented in the last section demonstrate the rapid 3D nanopositioning capability of this compact minimum-actuator magnetic levitator.

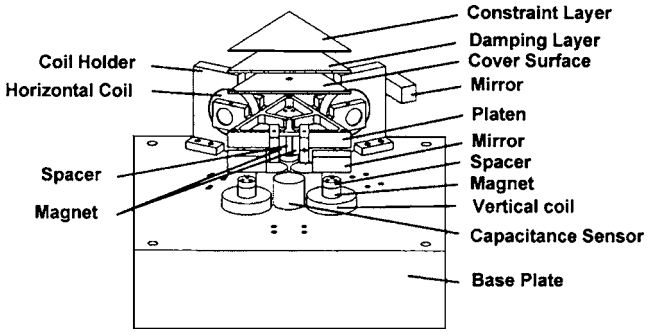

Fig. 2 Exploded view of the mechanical setup

2 Electromechanical Setup

Figure 2 shows an exploded view of the mechanical setup of the maglev stage. Its maglev single-moving part, namely the platen, consists of a triangular pocket-milled aluminum core, cylindrical magnet pieces for the six linear actuators, a viscoeleastic passive-damping layer, and a constraint layer.

2.1 Mechanical Setup. The total mass of the platen was found only 0.2126 kg by a precision balance. This small mass of the levitated platen resulted in low power consumption, 15 mW by each horizontal actuator in steady state and 320 mW by each vertical actuator to cancel the gravitational load. The triangular aluminum core has three pockets made by a CNC (computer numerical control) machine to reduce the moving-part mass. The three extruded arms hold the horizontal magnets. To be used as the target of the capacitance gap sensors, the bottom surface of the platen was ground to a surface roughness of 2.54 μm. Three plane mirrors were fixed on the sides of the platen by a 127 μm thick double-sided tape. A 1.52 mm thick C1002 shear damping sheet by E-A-R Specialty Composites and a stainless-steel constraint layer were attached on top of the platen core. This viscoelastic passive-damping mechanism damps out the vibration of the mechanical parts; the mechanical energy in the constraint layer's motion relative to the platen core is dissipated in the viscoelastic damping layer.

All the stationary parts such as six actuator coils, their holders, and capacitance sensors are mounted on a 55.4 mm thick aluminum base plate. This base plate thickness was decided to ensure a high natural frequency of 2.49 kHz determined by a finite-element (FE) analysis. The whole maglev system is placed on a precision optical table that reduces the vibration transmitted from the lab floor. Experiments showed that the optical table would transmit electronic noises, such as 60 Hz power-line noise to the base plate. Since this noise could greatly increase the noise level in the capacitance sensors, a piece of 254 μm thick plastic shim was inserted between the base plate and the optical table.

2.2 Linear Magnetic Actuators. The six-axis forces are generated by three horizontal actuators and three vertical actuators [20]. By controlling the currents through the coils in the six linear actuators independently, the platen can generate all 6-DOF motions. Figure 3 shows a schematic diagram of one of the six linear magnetic actuators in the maglev stage. Two cylindrical magnet pieces are placed with the same (south) poles facing against each other. A nonmagnetic spacer separates the two magnet pieces. The coil generates north and south poles governed by the right-hand rule. With the pole arrangement depicted in Fig. 3, upward axial force can be generated for the magnets with respect to the station-

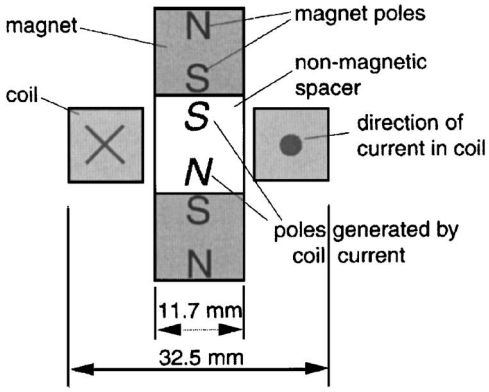

Fig. 3 Schematic diagram of a linear magnetic actuator. A Lorentz force is generated by placing the current-carrying coil in the magnetic field produced by the magnet assembly. The optimal thickness of 3.84 mm of the aluminum nonmagnetic spacer is exaggerated here for clarity.

ary coil. Changing the magnitude of current flowing through the coil controls the magnitude of the force. Reversing the direction of the coil current reverses the direction of the force.

Two magnets were glued with a 3.84 mm thick aluminum spacer whose thickness was determined to generate the maximum force [21]. The magnet assembly was fixed inside two coaxial circular holes on the extruded arms of the platen. For vertical actuators, the magnets were glued on aluminum spacers with three tapped holes. Each spacer was then fastened to the bottom surface of the platen with three screws. In the magnetic actuators, each cylindrical neodymium-iron-boron (NdFeB) magnet with energy product ($BH_{\max}$) of 0.4 MJ/m^3 (50 MGOe) has the diameter of 11.684 mm and the height of 9.525 mm.

The coils for the actuators are made up of single-build AWG#21 (diameter = 0.724 mm) copper magnet wire with 179 turns each. The coils have the inner diameter of 12.2 mm, the outer diameter of 32.5 mm on average, and the height of 9.55 mm. The resistance and the inductance of a coil are 0.552 Ω and 0.5 mH. A professional coil manufacturer, WireWinders, made the coils, and ensured the inner diameter tolerance better than 25.4 μm. Vertical coils were glued with PC-7 epoxy on small aluminum spacers to be fastened on the base plate. Horizontal coils were first glued to the coil holders using a fixture we developed to precisely locate the coil. The coil holders were then screwed on the base plate.

The high precision required in assembly and machining in this maglev nanopositioning instrument necessitated an error analysis. Because the errors are accumulated or amplified where two or more parts are joined, we tried to minimize the part counts. We used the error transformation method to quantify the effects of individual error sources correctly and the accumulation of the errors [22]. The error matrices were revised while we performed design iterations. This error analysis estimated an assembly and machining tolerance no greater than 50 μm in the whole mechanical system [23].

3 Dynamic Modeling

A 3D FE model of the mechanical system was built using SolidWorks. The system parameters such as the center of mass (CM), inertia matrix, and natural frequencies were calculated with this FE model. As the lowest resonance frequency of the platen was found to be greater than 1 kHz, it was unlikely that control signals with an expected maximum bandwidth of 100 Hz would excite a resonance mode. Due to the noncontact nature of this maglev system, the open-loop damping and stiffness would be negligible. Thus, we chose to use a pure mass model in the platen

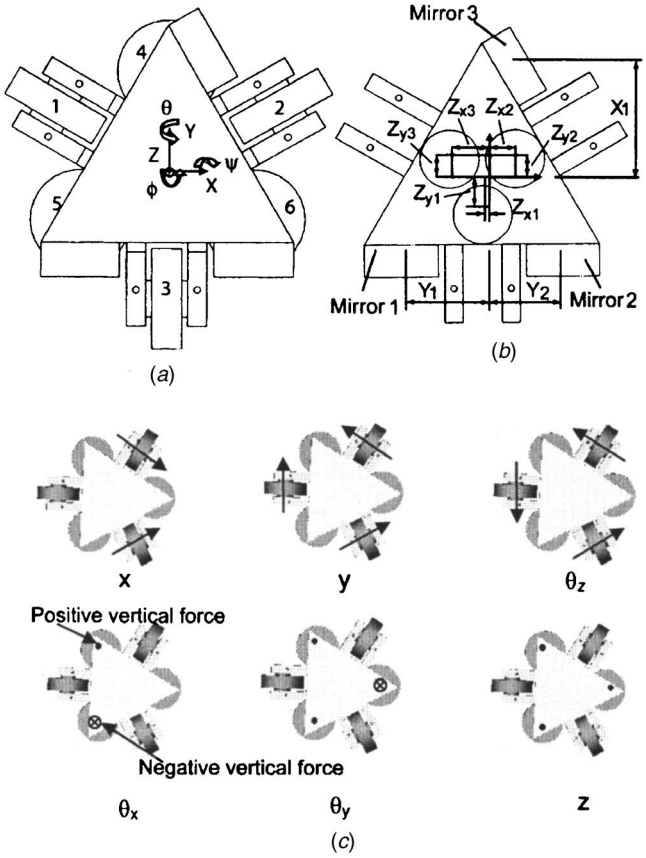

Fig. 4 (*a*) Definition of the axes and the numbering convention for each actuator. (*b*) Definition of the geometric parameters in the modal force and displacement transformations. (*c*) Conceptual actuator force allocation for 6-axis modal force generation.

rigid-body mode. Figure 4(*a*) gives the definition of the axes and the numbering convention for each actuator for dynamic modeling and control purposes.

3.1 Plant Transfer Functions. For translation, the equation of motion is as the following by the Newton's second law.

$$M\frac{d^2x}{dt^2} = f, \tag{1}$$

where M is 0.2126 kg. The expression for the modal force f will be derived in the following section. Thus, the open-loop plant transfer function for translational motion is

$$\frac{x(s)}{f(s)} = \frac{1}{0.2126s^2}. \tag{2}$$

Likewise, the open-loop plant transfer function for rotation is

$$\frac{\theta(s)}{T(s)} = \frac{1}{Is^2}, \tag{3}$$

where T refers to the torque about an axis, and I, the corresponding moment of inertia. The values of the moments of inertia were calculated as $I_{xx}=133$, $I_{yy}=122$, and $I_{zz}=236$ in 10^{-6} kg m^2 with SolidWorks. The coordinate axes we chose in Fig. 4(*a*) are almost principal, and all the products of inertia are less than 3% of the moments of inertia. Thus, we ignored the products of inertia.

3.2 Actuator Force Calculation and Experimental Verification. The force generated by the interaction between the permanent magnet and the coil current follows the Lorentz force equation, $\boldsymbol{f}=\int(\boldsymbol{J}\times\boldsymbol{B})\,dV'$, where $\boldsymbol{J}$ is the current density flowing through the coil, and $\boldsymbol{B}$ is the magnetic flux density produced by

the magnet. The magnet assembly produces a magnetic filed on the current-carrying coil placed concentric to the magnet assembly. The magnetic scalar potential, Ψ defined as $\boldsymbol{B}=-\mu_0\nabla\Psi$ was obtained by the following superposition integral [24].

$$\Psi = \int \frac{\rho_m(\boldsymbol{r}')dV'}{4\pi\mu_0|\boldsymbol{r}-\boldsymbol{r}'|}, \tag{4}$$

where ρ_m is the volume magnetic charge density in the magnet, and $\boldsymbol{r}$ and $\boldsymbol{r}'$ are the position vectors to an observer on the coil and an infinitesimal volume segment dV' in the magnet, respectively. Then, the resulting force can be found from the triple integral of $\boldsymbol{J}\times\boldsymbol{B}$ over the whole coil volume V'. Following is the full expression of this actuator force [21].

$$f_z = \left(\frac{J(\mu_0 M)}{4\pi}\right)\int_{c-w/2}^{c+w/2}\int_{z-h/2}^{z+h/2}\int_0^{2\pi} \times\frac{d}{dr}\left[\int_0^R\int_0^{2\pi}\frac{\rho}{\sqrt{(z-d/2)^2+r^2+\rho^2-2r\rho\cos(\theta-\phi)}}d\theta\,d\rho - \int_0^R\int_0^{2\pi}\frac{\rho}{\sqrt{(z+d/2)^2+r^2+\rho^2-2r\rho\cos(\theta-\phi)}}d\theta d\rho\right] \times r\,d\phi\,dz\,dr. \tag{5}$$

A MATHCAD code we wrote evaluated the above integration. Because of the difficulty in deriving a closed-form expression from Eq. (5), we chose to calculate the force with respect to a set of given values of z, and used the "polyfit" command in MATLAB to obtain a polynomial expression in a least-square sense. Equation (6) is the expression for the vertical actuator force.

$$f_z(z) = (-16938z^2 + 0.83895)\cdot i, \tag{6}$$

where i is the current through the coil, and z is the axial displacement of the magnet assembly from the center of the coil. Because the maximum displacement z is 300 μm, the first term in Eq. (6) is negligible compared to the second term. In other words, the actuator force f_z does not significantly depend on the actual displacement of the magnets inside the coil. Hence, for simplicity, a linear relation $f_z=k_f i$ is used to calculate the current required to generate a given force with the force constant k_f = 0.83895 N/A for the vertical actuators. The force constant for the horizontal actuators is twice as large as that of the vertical actuators since there are two magnet pieces in the horizontal actuators. The total vertical force with a nominal 1 A current in each of the three vertical coils is 2.52 N which is sufficient to levitate the platen mass of 0.2126 kg against the gravity. The maximum coil current delivered by a power amplifier was set as 2.5 A, which can provide additional 2 g (20 m/s^2) acceleration in the vertical direction and a 1.5 g (15 m/s^2) acceleration in the horizontal direction.

Experiments were performed to verify the analysis, especially the value of the force constant in Eq. (5). Various deadweights were placed as payload on the platen while the stage was operational in closed loop. A plot of desired current to maintain position versus applied payload is shown in Fig. 5. The small circles shown on the plot are the experimental data points and the straight line is their least-square fit by MATLAB. Note the clear linear relation between the coil current and the actuation in the figure. The slope of the line was found to be 0.7982 N/A, and the offset of −2.097 N canceled the gravitational load to the platen mass of 0.2126 kg. The error between empirical and theoretical values is less than 5%. The possible reason of the error may be inaccurate reading of data due to continuous fluctuation in current while in closed loop.

3.3 Modal Force Transformation. Let us define the six independent actuator forces to be f_1, f_2, and f_3 as the forces generated by the horizontal actuators, and f_4, f_5, and f_6 generated by the vertical actuators, following the numbering convention in Fig. 4(*a*). In Eqs. (2) and (3) the forces/torques act at the platen CM and are called modal forces/torques. We need to allocate these modal forces/torques to the six actuator forces. Figure 4(*c*) illustrates a conceptual force allocation. By applying six equilibrium conditions around the platen CM, we derived the following modal force transformation matrix.

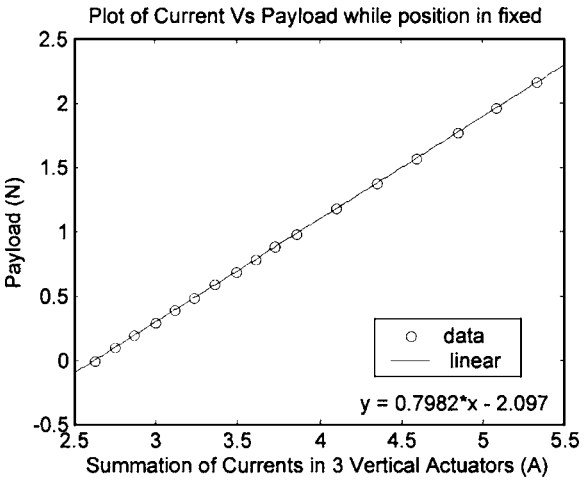

Fig. 5 Plot of payload vs current required to maintain the position

$$\begin{bmatrix} f_z \\ \tau_y \\ \tau_x \\ f_x \\ f_y \\ \tau_z \end{bmatrix} = \begin{bmatrix} 0 & 0 & 0 & 1 & 1 & 1 \\ 0 & 0 & 0 & l_{3x} & l_{1x} & -l_{2x} \\ 0 & 0 & 0 & l_{3y} & -l_{1y} & -l_{2y} \\ -\cos 60^\circ & -\cos 60^\circ & 1 & 0 & 0 & 0 \\ -\cos 30^\circ & \cos 30^\circ & 0 & 0 & 0 & 0 \\ l_{6z} & l_{5z} & l_{4z} & 0 & 0 & 0 \end{bmatrix}\begin{bmatrix} f_1 \\ f_2 \\ f_3 \\ f_4 \\ f_5 \\ f_6 \end{bmatrix}, \tag{7}$$

where geometric parameters (l's) represent the moment arms for the modal torques. For instance, l_{1x} is the distance in the x axis from the first actuator to the y axis. The zeros in the top-left and bottom-right parts of this transformation matrix reveal the intended independence between the vertical modes and the horizontal modes.

3.4 Modal Displacement Transformation. Similarly to the modal force transformation, a modal displacement transformation matrix was derived to relate the sensor measurements to the position of the platen CM. An Agilent Technologies interferometer system gives a 3-DOF position information of the maglev stage, i.e., translations in x and y and rotation around the z axis. The laser head (Model 5517D by Agilent) produces a 632 nm HeNe laser beam. The laser axis board (Model 10897B by Agilent) gives 35-bit displacement data with 0.6 nm resolution and 24-bit velocity data at a 10 MHz update rate. Three capacitance sensors (Model 2810 probes and Model 3800 electronics by ADE) fixed on the base plate are used to measure the translation in z and rotations around the x and y axes. The choice of capacitance sensors in the vertical mode was due to a relatively loose requirement of vertical position resolution and inconvenience in the placement of optical parts beneath the moving stage. As it can be seen in Sec. 5, the large noise of our capacitance sensors contributes to the lower resolution of the z axis motion.

With the definitions of the geometric parameters shown in Fig. 4(*b*), the displacement transformation matrix was derived to be

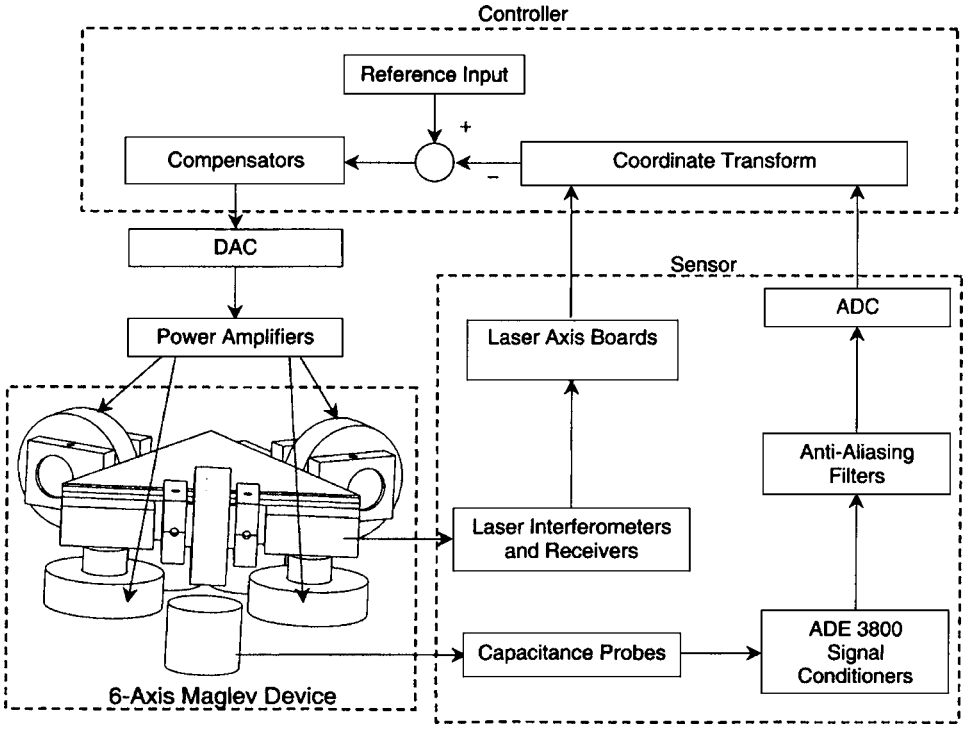

Fig. 6 Control loop of the maglev system

$$\begin{bmatrix} y_1 \\ y_2 \\ x_1 \\ u_1 \\ u_2 \\ v_1 \\ z_1 \\ z_2 \\ z_3 \end{bmatrix} = \begin{bmatrix} 1 & 0 & -Y_1 & 0 & 0 & 0 & 0 & 0 & 0 \\ 1 & 0 & Y_2 & 0 & 0 & 0 & 0 & 0 & 0 \\ -\frac{1}{2} & -\frac{\sqrt{3}}{2} & X_1 & 0 & 0 & 0 & 0 & 0 & 0 \\ 0 & 0 & 0 & 1 & 0 & -Y_1 & 0 & 0 & 0 \\ 0 & 0 & 0 & 1 & 0 & Y_2 & 0 & 0 & 0 \\ 0 & 0 & 0 & 0 & 1 & -X_1 & 0 & 0 & 0 \\ 0 & 0 & 0 & 0 & 0 & 0 & -Z_{y1} & Z_{x1} & 1 \\ 0 & 0 & 0 & 0 & 0 & 0 & Z_{y2} & -Z_{x2} & 1 \\ 0 & 0 & 0 & 0 & 0 & 0 & Z_{y3} & Z_{x3} & 1 \end{bmatrix} \begin{bmatrix} y \\ x \\ \phi \\ u \\ v \\ r \\ \psi \\ \theta \\ z \end{bmatrix}, \tag{8}$$

where y_1, y_2, and x_1 are the horizontal position measurements and u_1, u_2, and v_1 are the horizontal velocity measurements by the laser interferometers, and z_1, z_2, and z_3 are the vertical position measurements by the capacitance sensors. On the right-hand side of this transformation, y, x, z, ψ, θ, and ϕ are the six-axis modal displacement variables, and u, v, and r are the horizontal velocity variables of the platen CM.

With the dynamic model of the maglev system, the actuation force calculation, and the modal force and displacement transformations derived in this section, we were ready to design and implement a control system.

4 Control System

By Earnshaw's theorem, 6-DOF magnetostatic levitation in free space is inherently unstable because the permeability μ of any material is always greater than that of free space μ_0 [25]. Thus, six independent lead-lag controllers were designed and implemented for each of the six axes to stabilize the maglev system. With the modal force and displacement transformations applied, the whole maglev system can be considered a collection of six independent single-input-single-output (SISO) systems. The design of six independent SISO controllers can be easily implemented into our electrical system without overloading the processor.

We used the MATLAB RL (root-locus) tool to select the control parameters. The damping ratio ζ was chosen to be 0.7 and the phase margin, 52° at a crossover frequency of 50 Hz. Equation (9) is the lead-lag compensator designed for the z axis motion control.

$$G_z(s) = \frac{8.7315 \times 10^4 (s+135)(s+11)}{s(s+1385)} \tag{9}$$

The free pole at the origin in the s-plane eliminated the steady-state error. By using the zero-order-hold (ZOH) method with a 5 kHz sampling rate, this continuous model was converted to a discrete-time model

$$G_z(z) = \frac{8.7315 \times 10^4 (z-0.9767)(z-0.9978)}{(z-1)(z-0.758)}. \tag{10}$$

We used the same controller for the x and y axis motion control. The controllers for the three rotational axes have the same pole-zero locations with the controller gains of 96.872, 54.575, and 50.221 N for ϕ, ψ, and θ, respectively.

We implemented the control laws in real-time C on a digital signal processor (DSP) board (Model 4284 by Pentek), and developed a user interface on a VME PC (Model 7751 by VMIC) in C++. A timer routine measures the execution time of the control routine. It shows that in every 200 μs sampling period, approximately 70 μs is used for the real-time control, and the rest of the sampling period is used for nontime-critical background routines such as transferring and saving data. Thus, the present instrumentation possesses the computing power to implement more complicated control algorithms. Figure 6 shows the overall control loop of the maglev system.

Any dynamic coupling among the vertical modes and the horizontal modes may create unwanted erroneous motions. This unmodeled dynamics may degrade the stability and transient performance of the control system [15]. Therefore, in the design phase, the six magnetic actuators were intentionally placed to minimize

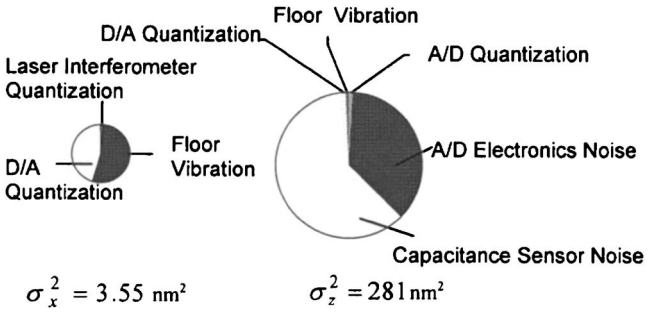

Fig. 7 Noise contributions from various sources (*a*) in the horizontal modes, and (*b*) In the vertical modes

dynamic coupling. To minimize the coupling between vertical and horizontal motion, we implemented a feedforward compensation strategy into our control system. Details on this feedforward compensation strategy can be found in [17].

5 Noise Analysis

The positioning capability is largely affected by the noise performance of individual components in the system. The significant noise sources include electronics noise, floor vibration, analog-to-digital (A/D) and digital-to-analog (D/A) quantization, and laser interferometer quantization. In the control loop, each noise source makes its own contribution to the final position noise. Since all the noises are considered as random signals, a stochastic system analysis method is used to model and predict the noise effects [26]. We present the analysis of the position noise in x in this section. We also use the noise analysis for the selection of the optimal control bandwidth.

5.1 Noise Components and their Propagation. In our noise/disturbance propagation model, the disturbance W_d enters the control loop as an additive force input to the plant. It includes the disturbance from floor vibration and D/A quantization. The sensor noise V_n includes sensor electronics noise, A/D quantization, and A/D electronics noise. For the measurements in the x and y axes, we consider the quantization noise from the laser interferometry. We assume that all the noises in this model are zero-mean white

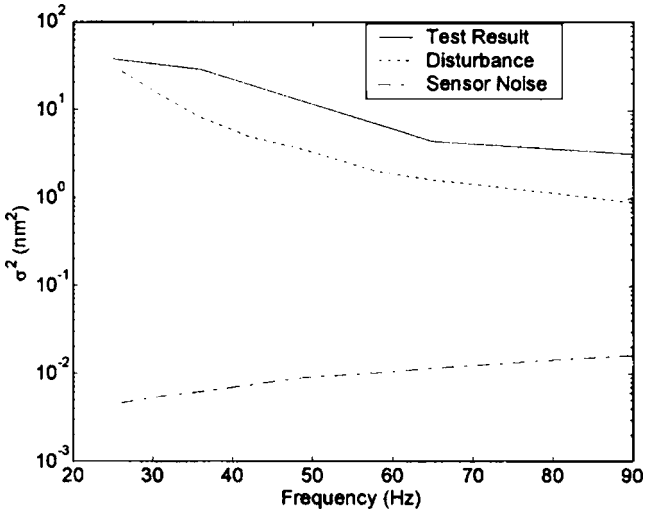

Fig. 8 Convariances of the theoretical sensor noise and disturbance, and an empirical result with respect to the crossover frequency in the horizontal modes. To find the total theoretical noise convarience, the two components (disturbance and sensor noise) should be added. Note that the magnitude is in a logarithmic scale.

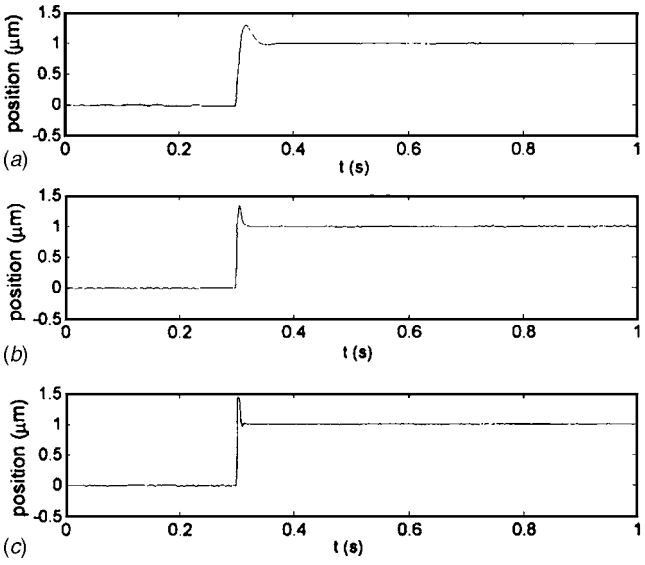

Fig. 9 1 μm step responses in *x* with crossover frequencies at (*a*) 25 Hz, (*b*) 65 Hz, and (*c*) 90 Hz

Gaussian noises (WGNs). Each WGN is modeled to pass through a first-order low-pass shaping filter before it enters the control loop. The cutoff frequencies of these shaping filters were chosen empirically at 500 Hz, an order higher than the control bandwidth.

Defining Δ to be the position resolution of the laser interferometer system, the covariance of the laser interferometry quantization noise is given by [27]

$$\sigma_{\text{laser}}^2 = \frac{\Delta^2}{12} = \frac{0.6^2}{12} = 0.03\ \text{nm}^2/(\text{rad/sample}), \qquad (11)$$

where $\Delta = 0.6$ nm from the specifications of the laser interferometry system.

The D/A quantization noise can be calculated similarly. If we define the voltage quantization as Δv, then the covariance of the force is given by

$$\sigma_{\text{D/A}}^2 = \frac{0.84^2 \Delta v^2}{12} = 1.37 \times 10^{-9}\ \text{N}^2/(\text{rad/sample}), \qquad (12)$$

where $\Delta v = 10/2^{16} = 1.53 \times 10^{-4}$ V with the 16-bit D/A resolution and the ±5 V D/A output swing. The factor of 0.84 is the gain from the D/A output to the force generated by the horizontal

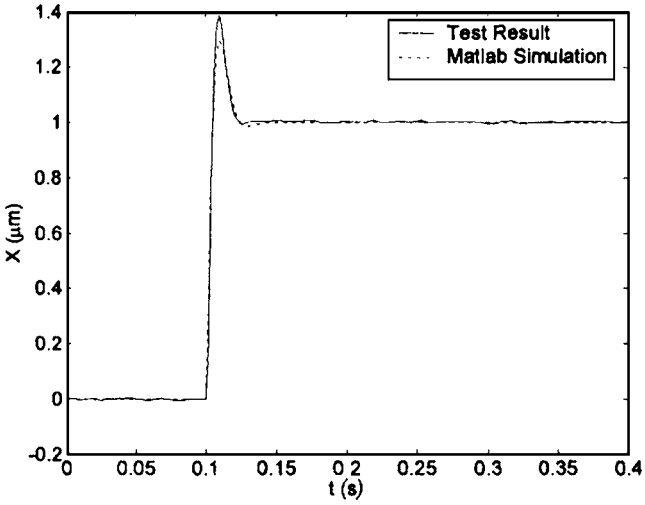

Fig. 10 1 μm step responses in *X* by a MATLAB simulation and an experiment

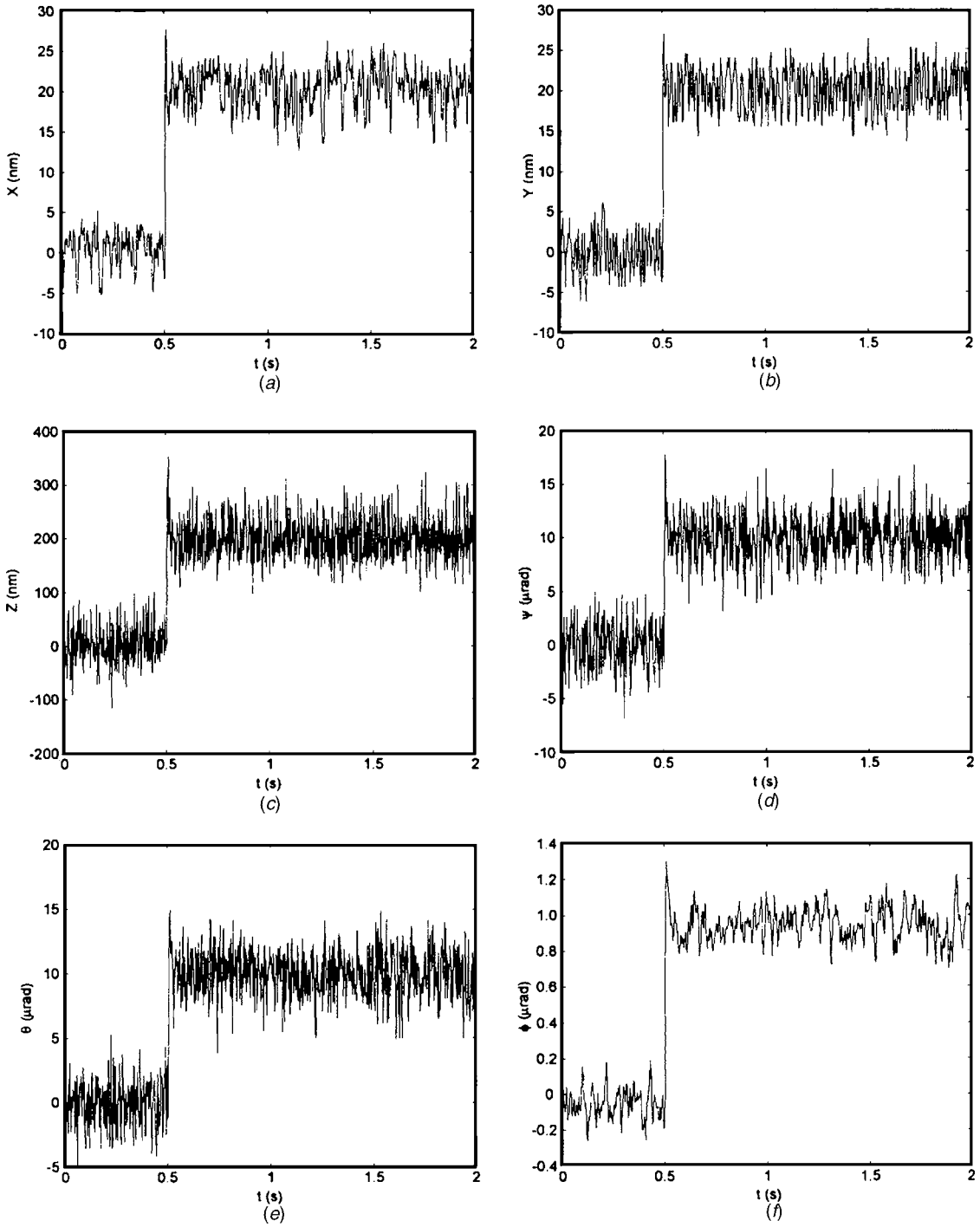

Fig. 11 Step responses in all six axes with step sizes of (*a*) 20 nm in *x*, (*b*) 20 nm in *y*, (*c*) 0.2 μm in *z*, (*d*) 10 μrad in ψ, (*e*) 10 μrad in θ, and (*f*) 1 μrad in ϕ

actuators.

The floor vibration transmitted through the optical table was measured and recorded by a precision accelerometer (Model 393C by PCB Piezotronics) with a storage oscilloscope (Model 54624A by Agilent). The covariance of the floor vibration in the x axis on the optical table is found to be 3.99×10^{-5} N^2/(rad/sample).

Equation (13) below was used to convert the above noise covariances to the equivalent continuous-time spectral density S. The sampling rate is 5 KHz.

$$S=\left(\frac{\sigma^2}{\text{rad/sample}}\right)\left(\frac{\text{s}}{5000\ \text{samples}}\right)\left(\frac{2\pi\ \text{rad/s}}{\text{Hz}}\right), \qquad (13)$$

where σ^2 represents one of the noise covariances obtained previously and equals to the discrete-time spectral density. Then, the following Eqs. (14) and (15) give the relationship between the spectral density of the noise component and its contribution to the covariance of the collective position noise [26].

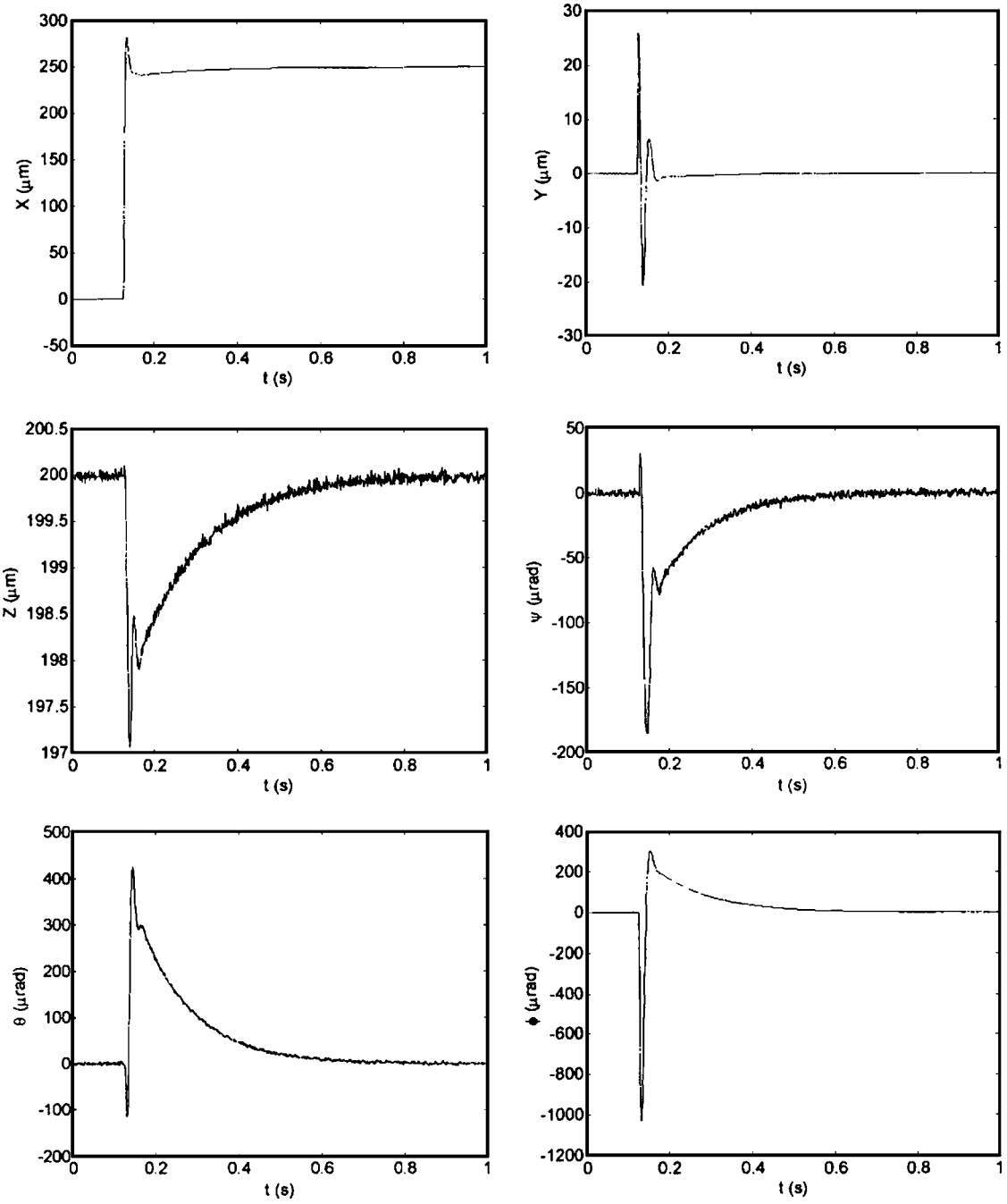

Fig. 12 Extended-range 250 μm step response in *x* and disturbed motions in all the other axes

$$\sigma_{x,n}^2 = \frac{S_n}{2\pi}\int_{-\infty}^{\infty}\left|\frac{-\alpha G_c(j\omega)/M}{(j\omega+\alpha)((j\omega)^2+G_c(j\omega)/M)}\right|^2 d\omega \qquad (14)$$

$$\sigma_{x,w}^2 = \frac{S_w}{2\pi}\int_{-\infty}^{\infty}\left|\frac{\beta/M}{(j\omega+\beta)((j\omega)^2+G_c(j\omega)/M)}\right|^2 d\omega, \qquad (15)$$

where $G_c(s)$ is the transfer function of the controller. Evaluating these integrals using MATHCAD yielded the noise contributions from each noise/disturbance source as shown in Fig. 7(*a*). Similarly, we calculated the noise contributions in the vertical axis as shown in Fig. 7(*b*). This noise analysis showed that the major noise components in the horizontal and vertical modes were the floor vibration, and the capacitance sensor and A/D electronic noises, respectively [21]. Thus, the floor vibration should be isolated more effectively, and quieter A/D converters and capacitance sensor electronics should be employed for further reduction of position noise.

5.2 Selection of the Optimal Control Bandwidth. According to Eqs. (14) and (15) from the noise/disturbance propagation model, the noise level is related to the transfer function $G_c(s)$. Therefore the selection of the crossover frequency based on this noise/disturbance propagation model developed in the previous section is an essential task to optimize the closed-loop system's noise performance and transient response. By using Eqs. (14) and (15), we could predict the noise level with controllers with various crossover frequencies. Figure 8 shows both theoretical and experimental results for the noise/disturbance level with respect to the crossover frequency in the horizontal axis. We can clearly see the

opposite effects of the crossover frequency on the disturbance and the sensor noise as predicted. In the horizontal modes, the disturbance is greater than the sensor noise by an order of 2 or 3. As a result, the overall position noise is smaller at a higher crossover frequency.

The experimental data (the solid line) in Fig. 8 shows the same trend as the theoretical analysis (the addition of the dashed and dash-dotted lines) with a discrepancy of about 1 nm in terms of the position-noise standard deviation (σ). This underestimation of the position noise is believed to originate from the disregard of other minor error sources. The noise analysis in the horizontal modes suggests a higher crossover frequency be used to achieve a smaller position noise. A similar theoretical and experimental study for the vertical modes, where the sensor noise is dominant, suggests that a lower crossover frequency be chosen for a best noise performance.

Figure 9 shows experimental 1 μm step responses with the crossover frequencies at 25, 65, and 90 Hz. The settling times are about 70, 20, and 10 ms, respectively. As expected, a higher crossover frequency leads to a faster step response. Besides the noise and dynamic performances, another important consideration in the selection of the crossover frequency is the stability. If the crossover frequency were much lower than 25 Hz, the control system could not maintain the closed-loop system stable due to a low control gain. If the crossover frequency were much higher than 90 Hz, one of the system resonance modes would be excited resulting in large structural vibration. Therefore, we chose the optimal crossover frequences without losing the closed-loop stability for the horizontal and vertical modes at 90 and 25 Hz, respectively, after a careful engineering tradeoff study between the noise/disturbance performance and the closed-loop dynamic performance.

6 More Experimental Results

Figure 10 shows 1 μm step responses in x by a MATLAB simulation and an experiment with the controller designed in Sec. 4. The experimental result agrees very well with the simulation, which verifies the accuracy of our system model and the lack of unmodeled nonlinearities such as friction, stiction, or backlash in this maglev system. This fact signifies the utility of the precision maglev technology in nanopositioning applications.

Figure 11 shows small step responses and position noises in all six axes. As seen in the figure, the translational position resolution is better than 2 nm in x and y, and 25 nm in z. The lower z axis resolution stemmed from the larger capacitance sensor and A/D electronics noises. For rotational motions, the angular position resolution is about 2 μrad in ψ and θ, and 200 nrad in ϕ. Figure 12 provides a 250 μm step response in x. Because of the abrupt change in acceleration, small perturbed motions can still be seen in the other 5 axes. However, these perturbations die out quickly due to the controller actions in the other axes.

Additional reference trajectories were used to demonstrate the nanoscale motion-control capability of the maglev stage. Figure 13 presents the test results of a square-wave motion with an amplitude of 20 nm and a sinusoidal motion with an amplitude of 50 nm. The periods of the reference commands were 800 ms and 1 s, respectively. The maglev stage is capable of following fine commanded motion trajectories maintaining the same noise level.

Figure 14 shows a spherical motion generated to test the 3D motion capability. This hemispherical trajectory was generated by commanding, in every sampling period of 200 μs, x, y, and z that followed an equation of a spherical shell parameterized in time. The radius of the hemispherical shell shown in the figure is 50 μm, and each circular motion is separated by 0.5 μm in the vertical direction. It took merely ten seconds for the magnetic levitator to complete this 3D trajectory.

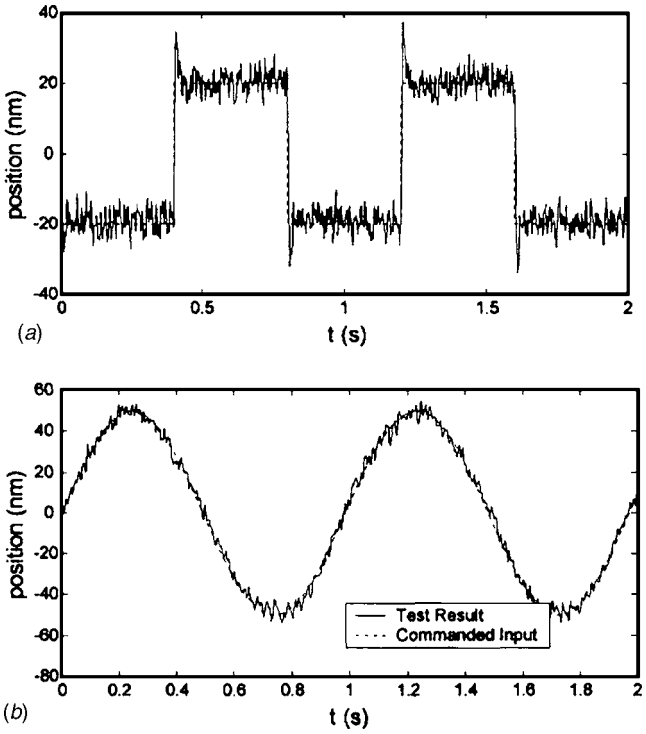

Fig. 13 (*a*) 20 nm amplitude square-wave motion in *x*. (*b*) 50 nm amplitude sinusoidal motion in *x*. The dashed lines represent the commanded input to generate the motion.

7 Conclusions

In this paper, we presented a novel magnetic levitator with 6-DOF nanoscale positioning capability. Possible applications include nanomanipulation, 3D rapid prototyping, manufacture of nanoscale structures, atomic-level manipulation, assembly and packaging of microparts, vibration isolation for delicate instruments, and seismic motion detection. Since no lubricant is needed, this maglev stage is suited in clean-room or vacuum environments in the nanotechnology and semiconductor manufacturing industries. Moreover, the simple mechanical structure without significant nonlinearity can reduce the manufacturing cost and improve the dynamic performance. The minimum number of actuators necessary and sufficient to generate all six-axis motions in our design led to a compact and light-weight moving part. The steady-state power consumption by the whole levitation system is only about a Watt.

Six linear magnetic actuators were incorporated to generate six independent Lorentz forces. A simple pure-mass model is cur-

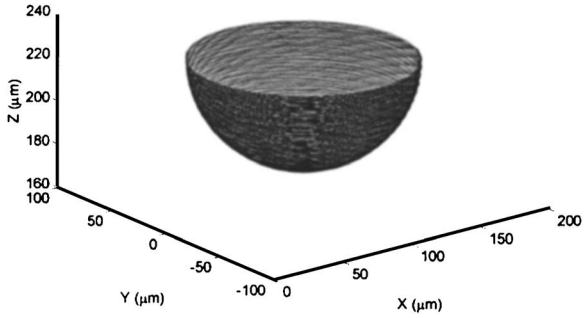

Fig. 14 3D spherical motion. The hemispherical shell has a radius of 50 μm, and each circular motion is separated by 0.5 μm in the vertical direction.

rently being used. After the modal force transformation and the modal displacement transformation were derived, six SISO lead-lag controllers were designed and implemented to stabilize each of the 6-axis motions.

A noise propagation model and a stochastic noise analysis helped to quantify the contributions from each noise source to the final collective position noise. The noise analysis suggested that we isolate the floor vibration more effectively and employ quieter A/D converters and capacitance sensor electronics for further reduction of position noise. The discussion on the selection of the optimal crossover frequency used the comparison in step responses and noise performances with various controllers. After considering the response speed and the noise level, we chose the crossover frequencies at 25 Hz in the vertical modes where the sensor and A/D electronics noises were dominant, and at 90 Hz in the horizontal modes where the floor vibration was dominant.

This maglev stage has a position resolution better than 2 nm in horizontal motion. The experimental step responses showed a tens-of-millisecond settling time on average. Several motion trajectories such as a long-distance step response, sinusoidal and square-wave trajectories, and a 3D spherical motion were presented to verify the maglev stage's capability in rapid extended-range 3D nanopositioning.

Acknowledgments

This material is based upon work supported by the National Science Foundation under Grant No. CMS-0116642. The authors thank H. Maheshwari for his contribution in the magnetic actuator force calculation.

References

[1] Sitti, M., 2001, "Survey of Nanomanipulation Systems," Proc. IEEE-NANO 2001, pp. 75–80.

[2] Sitti, M., and Hashimoto, H., 2000, "Controlled Pushing of Nanoparticles: Modeling and Experiments," IEEE/ASME Trans. Mechatron., **5**(2), pp. 199–211.

[3] Bauer, C., Bugacov, A., Koel, B. E., Madhukar, A., Montoya, N., Ramachandran, T. R., Requicha, A. A. G., Resch, R., and Will, P., 1998, "Nanoparticle Manipulation by Mechanical Pushing: Underlying Phenomena and Real-Time Monitoring," Nanotechnology, **9**(4), pp. 360–364.

[4] Taylor, R. M., 1994, "The Nanomanipulator: A Virtual-Reality Interface to a Scanning Tunneling Microscope," Ph.D. Dissertation, University of North Carolina at Chapel Hill, Chapel Hill, NC.

[5] Yu, M. F., Dyer, M. J., Rohrs, H. W., Lu, X.K., Ausman, K. D., Her, J. V., and Ruoff, R. S., 1999, "Three-Dimensional Manipulation of Carbon Nanotubes under a Scanning Electron Microscope," Nanotechnology, **10**(3), pp. 244–252.

[6] Requicha, A. A. G., Meltzer, S., Terán, A. F. P., Makaliwe, J. H., Sikén, H., Hsieh, S., Lewis, D., Koel, B. E., and Thompson, M. E., 2001, "Manipulation of Nanoscale Components with the AFM: Principles and Applications," Proc. IEEE-NANO 2001, pp. 81–86.

[7] Egshira, Y., Kosaka, K., Takada, S., Iwabuchi, T., Baba, T., Moriyama, S., Harada, T., Nagamoto, K., Nakada, A., Kubota, H., and Ohmi, T., 2001, "0.69 nm Resolution Ultrasonic Motor for Large Stroke Precision Stage," Proc. IEEE-NANO 2001, pp. 397–402.

[8] Jayawant, B. V., 1981, *Electromagnetic Levitation and Suspension Techniques*, Edward Arnold Ltd., London.

[9] Hajjaji, A. E., and Ouladsine, M., 2001, "Modeling and Nonlinear Control of Magnetic Levitation Systems," IEEE Trans. Ind. Electron., **48**(4), pp. 831–838.

[10] Takahara, K., 1988, "Development of a Magnetically Suspended, Tetrahedron-Shaped Antenna Pointing System," Proc. NASA CP-2056, 22nd Aerospace Mechanisms Symp., pp. 133–147.

[11] Gupta, A. A., Germann, L. M., and Medbery, J. D., 1991, "Six Degree-of-Freedom Magnetically-Suspended Fast Steering Mirror (MSFSM) Tracks Atmospheric Turbulence While Providing Focusing and Collimation Travel," Proc. 14th Annual AAS Guidance and Control Conference, AAS 91–039.

[12] Hollis, R. L., and Salcudean, S. E., 1993, "Lorentz Levitation Technology: a New Approach to Fine Motion Robotics, Teleoperation, Haptic Interface, and Vibration Isolation," Proc. 5th International Symposium on Robotics Research, pp. 1–18.

[13] Salcudean, S. E., Davis, H., Chen, C. T., Goertz, D. E., and Tryggvason, B. V., 1992, "Coarse-Fine Residual Gravity Cancellation System with Magnetic Levitation," IEEE International Conference on Robotics and Automation, pp. 1641–1647.

[14] Shan, X., Kuo, S.-K., Zhang, J., and Menq, C.-H., 2002, "Ultra Precision Motion Control of a Multiple Degrees of Freedom Magnetic Suspension Stage," IEEE/ASME Trans. Mechatron., **7**(1), pp. 67–78.

[15] Jung, K. S., and Baek, Y. S., 2002, "Study on a Novel Contact-Free Planar System Using Direct Drive DC Coils and Permanent Magnets," IEEE/ASME Trans. Mechatron., **2**(1), pp. 35–43.

[16] Chen, S. S., Busch-Vishniac, I. J., 1995, "A Magnetically Levitated, Automated, Contact Analytical Probe Tool," IEEE Trans. Semicond. Manuf., **8**(1), pp. 72–78.

[17] Kim, W.-J., and Trumper, D. L., 1998, "High-Precision Magnetic Levitation Stage for Photolithography," Precis. Eng., **22**(2), pp. 66–77.

[18] Holmes, M. L., 1994, "Analysis and Design of a Magnetically Suspended Precision Motion Control Stage," M.S. Thesis, University of North Carolina at Charlotte, Charlotte, NC.

[19] Holmes, M. L., Hocken, R., and Trumper, D., 2000, "The Long Range Scanning Stage: a Novel Platform for Scanned Probe Microscopy," Precis. Eng., **24**(3), pp. 191–209.

[20] Kim, W.-J., and Maheshwari, H., 2002, "High-Precision Control of a Maglev Linear Actuator with Nanopositioning Capability," Proc. of 2002 American Control Conference, pp. 4279–4284.

[21] Kim, W.-J., Gu, J., and Maheshwari, H., 2002, "Six-DOF Mechatronic Nanopositioning Device," Proc. 2nd IFAC Conference on Mechatronics Systems, pp. 909–914.

[22] Slocum, A. H., 1992, *Precision Machine Design*, Prentice-Hall, Inc., Englewood Cliffs, NJ, Chap. 2.

[23] Gu, J., 2003, "Development of a 6-Degree-of-Freedom Magnetically Levitated Instrument with Nanometer Precision," M.S. Thesis, Texas A&M University, College Station, TX.

[24] Haus, H. A., and Melcher, J. R., 1989, *Electromagnetic Fields and Energy*, Prentice-Hall, Inc., Englewood Cliffs, NJ.

[25] Earnshaw, S., 1842, "On the Nature of the Molecular Forces which Regulate the Constitution of the Luminiferous Ether," Trans. Cambridge Philos. Soc., **7**, pp. 97–112.

[26] Maybeck, P. S., 1979, *Stochastic Models, Estimation, and Control*, Academic Press, NY.

[27] Papoulis, A., 1991, *Probability, Random Variables and Stochastic Processes*, 2nd ed., McGraw-Hill Higher Education, NY.